Effect of a Dodecylsulfate-Modified Magnesium–Aluminum Layered Double Hydroxide on the Morphology and Fracture of Polystyrene and Poly(styrene-*co*-acrylonitrile) Composites

V. Realinho,[1] M. Antunes,[1] D. Arencón,[1] A. I. Fernández,[2] J. I. Velasco[1]

[1]*Centre Català del Plàstic, Departament de Ciència dels Materials i Enginyeria Metallúrgica, Universitat Politècnica de Catalunya, Colom 114, E-08222 Terrassa (Barcelona), Spain*
[2]*Departament de Ciència dels Materials i Enginyeria Metallúrgica, Universitat de Barcelona, Martí i Franqués 1, E-08028 Barcelona, Spain*

Received 3 July 2008; accepted 26 August 2008
DOI 10.1002/app.29288
Published online 25 November 2008 in Wiley InterScience (www.interscience.wiley.com).

ABSTRACT: Composites of polystyrene (PS) and poly (styrene-*co*-acrylonitrile) (SAN) containing a fraction of a dodecylsulfate-modified Mg–Al layered double hydroxide (LDH) were prepared by means of a melt-extrusion process. The structure and morphology were analyzed with wide-angle X-ray scattering and transmission electron microscopy, respectively. The X-ray spectra of the PS matrix composite displayed the diffraction peak characteristic of the hybrid LDH basal plane at $2\theta = 3.1$ deg. The SAN matrix composite did not exhibit such a diffraction peak. Both PS and SAN composites displayed an intercalated type of morphology with respect to the LDH platelets, as assessed by transmission electron microscopy. A plasticizing effect due to the hybrid LDH particles was observed for all composites and was supported by a decrease in the glass-transition temperature values and by Fourier transform infrared spectra. Besides tensile properties, the fracture toughness of the composites was compared with that of the pure polymers through the linear elastic fracture mechanics parameters. They were determined from fracture tests under a three-point-bending configuration. The results indicated that the effect of adding a small fraction of modified LDH particles to SAN caused an improvement in fracture toughness of 50% with respect to that of the pure polymer. Moreover, the relative increase in the fracture energy was about 200%. For PS matrix composites, both tensile properties and linear elastic fracture mechanics fracture parameters remained unaffected. These results were explained on the basis of the different plasticities developed by both polymers around the particles. © 2008 Wiley Periodicals, Inc. J Appl Polym Sci 111: 2574–2583, 2009

Key words: fracture; nanocomposites; polystyrene

INTRODUCTION

Despite all the thorough research work on polymer–clay nanocomposites in the last decade, only scattered investigations have considered the synthesis and characterization of polymer nanocomposites based on layered double hydroxides (LDHs).[1–10] A couple of works have focused on how LDH particles may affect some thermal and mechanical characteristics of the base polymers, such as the thermal stability and barrier properties of polymers used for packaging and medical applications,[11] electrical cable insulation and water impermeability,[12] flame retardancy,[13] and thermal conductivity,[14] or on how their presence alters the mechanical properties.[15,16]

LDHs, also known as anionic clays because of the presence of anions between the brucite-like layers, show the general formula $M^{2+}_{1-x}M^{3+}_{x}(OH)_2A^{-x/n}_{n}\cdot mH_2O$, where x has a value between 0.17 and 0.33.[17] Partial M^{2+}/M^{3+} substitution positively charges these brucite-like layers, which are charge-balanced by the presence of interlayer anions, which are normally a carbonate-type (CO_3^{2-}) in most of the samples found in nature. This particular structure results in strong interlayer electrostatic interactions between the layers, which make it difficult to exfoliate natural LDH platelets via normal procedures such as melt mixing. To weaken these electrostatic interactions and facilitate LDH delamination and polymer dispersion by conventional methods, their easy anionic interchange can be used to replace the original inorganic anions (e.g., carbonate with organic ones), creating hybrid LDH precursors with expanded layer distances, weakening layer-to-layer interactions, and ultimately promoting platelet delamination.[18] This increase also facilitates

Correspondence to: V. Realinho (vera.realinho@upc.edu).
Contract grant sponsor: Spanish Ministry of Science and Education; contract grant number: MAT2007-62956.

macromolecular intercalation during melt mixing, which, alongside the strong local shear and elongational stresses achieved during the process, may ideally produce platelet exfoliation, helping to create a nanocomposite type of material.

Glassy polymers such as polystyrene (PS) and poly(styrene-*co*-acrylonitrile) (SAN) exhibit mainly a brittle type of fracture, showing very low toughness values. This is especially noticeable in PS because of its high notch sensibility. SAN copolymers, although exhibiting enhanced tensile strength (σ_{max}) in comparison with PS, show similar fracture toughness (K_{Ic}) and fracture energy (G_{Ic}) values. Adding nanoclays or other nanoparticles to these glassy polymers could be a possible way of enhancing their K_{Ic} values; this could widen their applicability range and durability. In comparison with homologous microcomposites, the high specific surface area of nanoparticles promotes higher particle/matrix interface interaction; they not only act as a reinforcing agent, increasing stiffness and strength, but also locally affect the polymer morphology, enabling new mechanisms of energy dissipation that may enhance toughness.[19–25] Although most of the reported works regarding clay nanocomposites show that they have lower toughness values than their respective matrix polymers, Cohen and coworkers[26–28] and Giannelis and coworkers[29,30] found that some particulate-filled polymer nanocomposites show an increase in toughness in comparison with the respective neat polymer. They attributed this effect to the combined mechanisms of crack deflection and local plastic deformation of the polymer around the particles following debonding.

In this study, nanocomposites of PS and SAN were prepared through the melt mixing of the polymers with organically modified Mg–Al hydrotalcite (HT) particles. A linear elastic fracture mechanics (LEFM) analysis of the nanocomposites and pure polymers was carried out to determine the fracture parameters and clarify any possible reinforcement mechanisms induced by the LDH nanoparticles. The structure and morphology of the nanocomposites, as well as their thermal and mechanical properties, were also considered.

EXPERIMENTAL

Materials and compounding

The PS used, with the commercial trade name of Polystyrol 158K and with a melt flow index (MFI) of 3.0 g/10 min at 200°C and 5 kg, was supplied by BASF (Tarragona, Spain). Dow Plastics (Edegem, Belgium) provided SAN (Tyril 867E), a copolymer with a styrene content of 76% and an acrylonitrile content of 24% along with an MFI of 4.0 g/10 min at 230°C and 3.8 kg.

$Mg_6Al_2(OH)_{16}(CO_3)\cdot 4H_2O$, an HT with the commercial trade name Syntal HSA 696, was kindly supplied by Süd-Chemie (Toledo, Spain). The following anionic interchange procedure was performed on HT before melt compounding to increase the basal distance between the HT platelets and promote dispersion. First, to destabilize the whole HT crystal structure, an ionic interchange was performed between the CO_3^{2-} anions originally present between the HT platelets and Cl^- obtained from an HCl solution (pH = 4). After the addition of 100 g of HT to this acid solution, it was allowed to rest for 18 h at room temperature under an N_2 atmosphere. The precipitate obtained at the end of this procedure was then washed with water and placed in a sodium dodecyl sulfate (Sigma–Aldrich; purum ≥96%) solution to promote a second ionic exchange reaction, in this case by the interchange of chloride with dodecylsulfate (DDS) anions. This solution, kept under an N_2 atmosphere, was then stirred and heated at 75°C for 72 h. At the end, the excess of sodium dodecyl sulfate was removed with vacuum water filtration. The resulting organically modified hydrotalcite (oHT) was dried off in an oven at 80°C for 24 h and finally crushed into a powder with a mill.

Three different composites—5 wt % oHT–PS (PS-5), 5 wt % oHT–SAN (SAN-5), and 10 wt % oHT–PS (PS-10)—were prepared by the melt mixing of the respective polymer with the modified HT in a corotating twin-screw extruder (length/diameter = 36 and diameter = 25 mm) at a constant rotating speed of 110 rpm. At the end, the 3-mm-diameter circular cross-section extrudates were water-cooled and pelletized. MFI values of several melt-compounded samples are shown in Table I.

Square and circular plates with nominal thicknesses of 1 and 3.4 mm, respectively, were compression-molded in a hot-plate press after the drying of the previously extrusion-compounded pellets in an oven for 6 h at 90°C. Tensile specimens (ISO 527-Type 1B) were directly obtained from the square plates with a mechanical saw. Meanwhile, single-edge notched bend (SENB) fracture specimens were prepared by direct cutting of the circular plates and

TABLE I
Basic Characterization Results of the Pure Polymers and Respective Composites

Material	oHT weight content (%)	MFI (g/10 min)	Vicat softening temperature (°C)	T_g (°C)
PS	—	19.6	106.9	93.1
PS-5	5.2	20.3	103.2	89.8
PS-10	11.6	22.7	101.1	88.1
SAN	—	7.9	105.9	92.7
SAN-5	5.3	9.0	102.5	88.5

insertion of a central notch in the narrowest side with a 45° V notch broaching tool. Before each test, the notches were sharpened with a razor blade.

Testing procedure

Infrared spectra were obtained with a Nicolet 510 M spectrometer. Specimens were prepared by the application of 10 tons over solid pellets of a mix of the materials (3 wt % each) and dry KBr. Fourier transform infrared (FTIR) spectra were collected with a 4-cm^{-1} spectral resolution with 36 scans.

Wide-angle X-ray scattering measurements were performed with a Siemens D-5000 X-ray diffractometer. Radial scans were taken from 0.5 to 60° with a step size and step time of 0.020° and 5 s, respectively, with filtered Cu Kα radiation ($\lambda = 0.154$ nm).

The MFIs of the composites were determined at 210°C and a load of 10 kg according to the standard ISO-1133 with a Ceast 684 extrusion plastometer with a die diameter of 2.095 mm and a length of 8 mm.

The Vicat softening temperature was determined on flat specimens (1-cm^2 surface and 3.4-mm thickness) according to method A of the ISO-336 standard (10 N load and heating rate of 50°C/h).

Differential scanning calorimetry (DSC) measurements were performed with a PerkinElmer Pyris 1 calorimeter. Calibration was done with In and Pb standards. Samples, directly obtained from the compression-molded circular plates, were prepared with a weight between 11 and 14 mg. Once each sample's thermal history was erased (4 min at 200°C), a cooling run was performed from 200 to 25°C at a cooling rate of 20°C/min, and this was followed by a final heating cycle from 25 to 200°C at 20°C/min. All runs were carried out under a stream of dried nitrogen.

Tensile specimens (type 1B in the ISO-527 standard) were directly cut from the 1-mm-thick compression-molded plates. A Galdabini Sun 2500 universal testing machine with a 1 kN load cell, as well as a video extensometer to measure specimen deformation, was used in all tensile measurements. Tests were performed at a constant crosshead speed of 1 mm/min. From the experimentally recorded stress–strain curves, the values of the Young's modulus (E), σ_{max}, and elongation at break (ε_b) were obtained for each material.

LEFM tests were carried out with a three-point-bending configuration on SENB specimens at a constant crosshead speed of 1 mm/min and room temperature (20 ± 2°C). The specimen thickness was kept constant (3.4 mm), whereas the length and width, as well as the test span, were chosen to fulfill the requirements of the ESIS standard protocol.[31] A V-shaped notch was centrally inserted and sharpened with a razor blade before each test. The typical value of the initial crack length was 5.5 mm.

Qualitative information about the dispersion degree of the HT platelets in each polymer was assessed with a JEOL 1200-EXII transmission electron microscope on ultramicrotomed sheets with a typical thickness of 30–100 nm.

The fracture surfaces were analyzed with scanning electron microscopy to elucidate the morphological aspects related to the mechanisms of polymer deformation and fracture. A JEOL JSM-5610 scanning electron microscope was used after the fracture surfaces were made conductive by the sputtering deposition of a thin layer of gold–palladium.

RESULTS AND DISCUSSION

Chemical characteristics

FTIR spectra of both the unmodified HT and oHT, shown in Figure 1, present a broad band around 3470 cm^{-1}, which is explained by the superpositioning of the stretching vibration bands of Al—OH, Mg—OH, and O—H, this last one corresponding to the water molecules present between the layers. In HT spectra (Fig. 1), a shoulder can also be observed around 3000–3100 cm^{-1} and is attributed to interlayer interactions between hydroxyl groups and carbonate anions. The broad signal observed around 1650 cm^{-1} corresponds to the interlayer water molecules. The strong peak at 1370 cm^{-1} has been assigned to the asymmetric stretching of the interlayer carbonate anions.[12] In addition, different signals associated with the stretching vibration modes of Al—OH (980, 800, and 590 cm^{-1}) and Mg—OH (690 and 450 cm^{-1}) have also been observed.[32] Because of the presence of DDS, oHT displays the characteristic C—H aliphatic chain stretching vibration bands at 2958, 2925, and 2852 cm^{-1} as well as S—O at 1225 cm^{-1} (Fig. 1).[12] Also, the S—O bending vibration modes appear around 1067 and 1470 cm^{-1}.

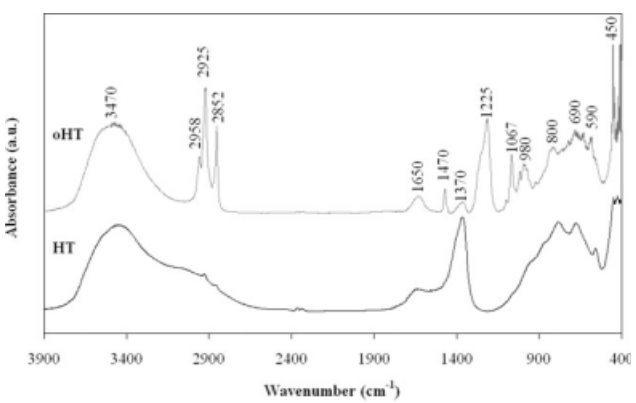

Figure 1 FTIR spectra of pure Mg–Al HT and oHT.

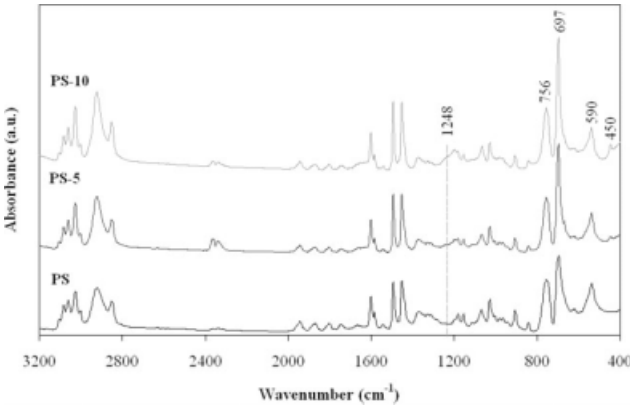

Figure 2 FTIR spectra of PS and PS–oHT nanocomposites.

Moreover, because in oHT the carbonate anions are ionically interchanged by the DDS ones, the intensity of the previously mentioned stretching peak at 1370 cm^{-1} is considerably weaker than that in unmodified HT.

The FTIR spectra of PS, SAN, and their respective oHT composites are shown in Figures 2–5. All the composite spectra display the characteristic base polymer absorption bands, the aromatic and aliphatic C—H stretching vibration bands appearing between 3130 and 2810 cm^{-1}. In the case of the SAN composite, the stretching vibration of the acrylonitrile (CN) group appears at 2238 cm^{-1}. Meanwhile, weak aromatic overtone and combination bands can also be observed between 2000 and 1680 cm^{-1}, with aromatic ring C=C stretching vibrations bands being observed in the spectral region from 1630 to 1570 cm^{-1}.[33] The peak at 756 cm^{-1} has been assigned to benzene's out-of-plane C—H bending, and the bands at 697 and 540 cm^{-1} have been assigned to the aromatic ring out-of-plane deformation.[33–35] The characteristic HT vibration peaks can also be observed in the FTIR spectra of the composites, the most characteristic of which are the S—O stretching vibration band at 1248 cm^{-1} and the Mg—OH vibration at 450 cm^{-1}.

Beside the presence of the previously mentioned characteristic vibration bands for both the polymers and hybrid HT, there is a remarkable increase in the intensity of the out-of-plane ring deformation band located at 697 cm^{-1} (Figs. 3 and 5). This effect can be explained by the weak interactions between oHT's aliphatic C_{12} chain and the aromatic ring, which disrupt the secondary bonds that hold the polymer chains altogether and ultimately create more room for aromatic ring motion. Related to this, the plasticizing effect of different low-molecular-weight aliphatic compounds (metal soaps, waxes, etc.) has been reported.[36]

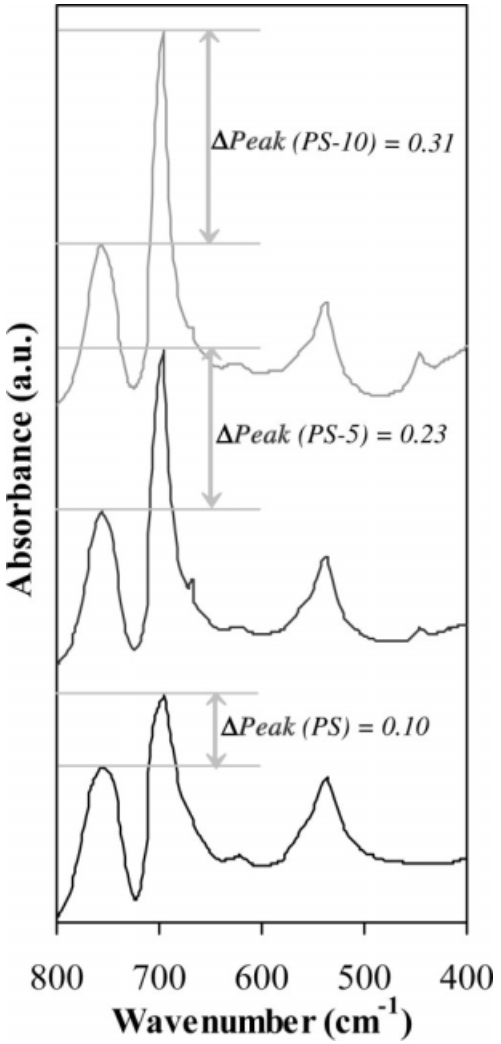

Figure 3 FTIR spectra of PS and PS–oHT nanocomposites (400–800 cm^{-1}).

Structure

The expansion of the interlayer distance caused by HT's ion-exchange modification as well as oHT's

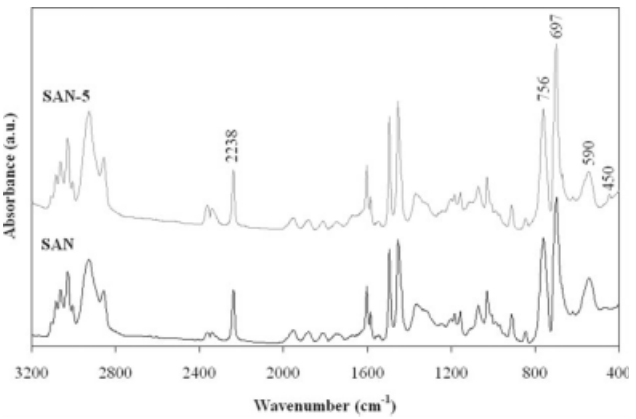

Figure 4 FTIR spectra of the SAN copolymer and SAN–oHT nanocomposite.

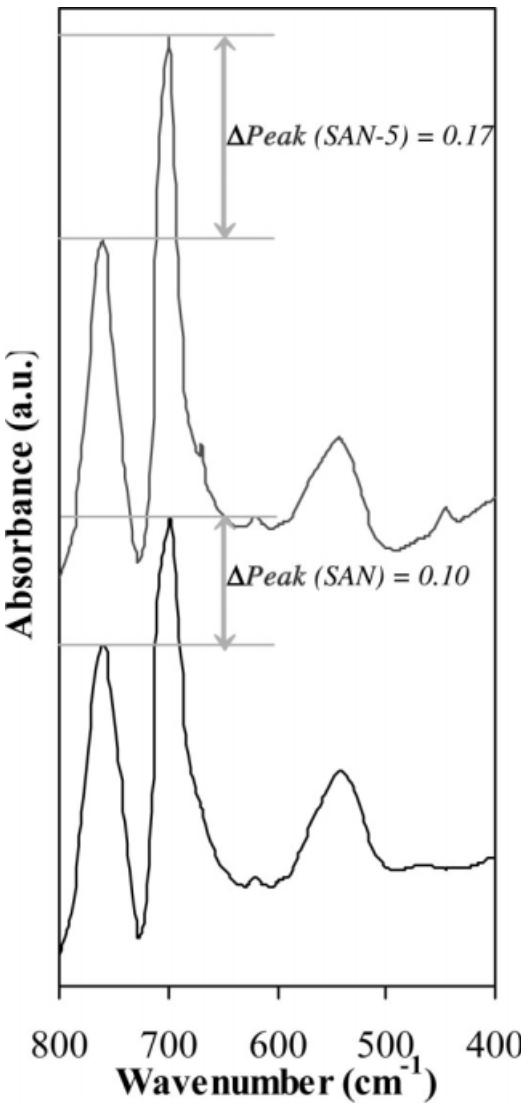

Figure 5 FTIR spectra of the SAN copolymer and SAN–oHT nanocomposite (400–800 cm^{-1}).

lamellar inner crystallite disposition was studied with wide-angle X-ray scattering. The HT characteristic diffraction peaks (Fig. 6) move toward lower diffraction angles after modification, and this indicates an expansion of the interlayer distance. Although for unmodified HT the (003) basal plane appears at $2\theta = 11.4°$, for oHT it appears at 3.3°; they correspond to interlayer distances ($d_{(003)}$) of 0.78 and 2.67 nm, respectively.

In PS–oHT composites, the oHT basal plane appears at $2\theta = 3.1°$ as a broad, relatively intense peak. Nevertheless, in the SAN–oHT composite, this peak practically disappears, with only a slight shoulder being noticed; this indicates crystallographic structural changes in oHT and, in particular, the loss of the particles' characteristic inner crystal order. A possible explanation for this remarkable difference in structure between the two composites may lie in their different viscosities, which are easily assessed from the MFI values shown in Table I. Compared to that of PS, the higher viscosity of SAN promotes higher local shear forces during melt processing,[37] promoting oHT particle dispersion/disorder. Additionally, it is possible that the higher polarity of SAN, due to the presence of the acrylonitrile (—CN) functional group, can also contribute to oHT dispersion and a higher crystallite disorder because of higher local interactions; nonetheless, this second effect seems negligible because the reduction in the glass-transition temperature (T_g) values (Table I) is more in accordance with somewhat weak interactions.

The transmission electron microscopy analysis revealed the presence of oHT primary particles in the PS composites (Fig. 7). A so-called crystalline ordered inner structure can be observed for the oHT crystallites. On the contrary, oHT intercalated particles seem to have a less ordered inner structure in the SAN composite than that observed in the PS ones. Even a few exfoliated platelets can be ascertained in the surroundings of the intercalated particles. This may be due to the higher viscosity of SAN versus PS, which would promote higher local shear forces during melt compounding, promoting particle dispersion/crystallite disorder. The former observation is in accordance with the disappearance of the $d_{(003)}$ diffraction peak for the SAN composite because such disorder would lead to the loss of oHT's crystallographic regularity and thus the peak's absence.

Thermal properties

A significant decrease in the polymer T_g value was observed by DSC for all the composites versus those of the respective pure polymers. The Vicat softening temperatures (Table I) are in good agreement with

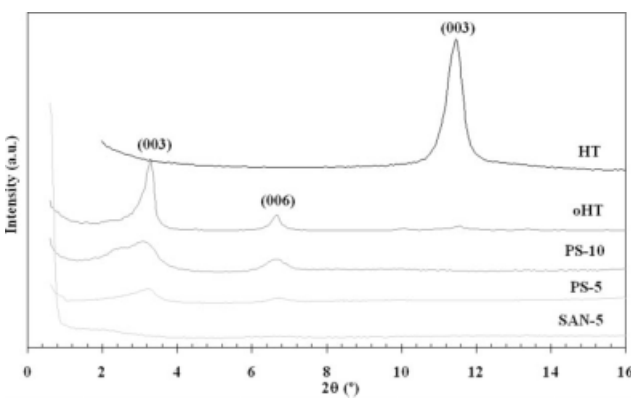

Figure 6 X-ray diffraction spectra of unmodified HT, oHT, and PS-10, PS-5, and SAN-5 nanocomposites.

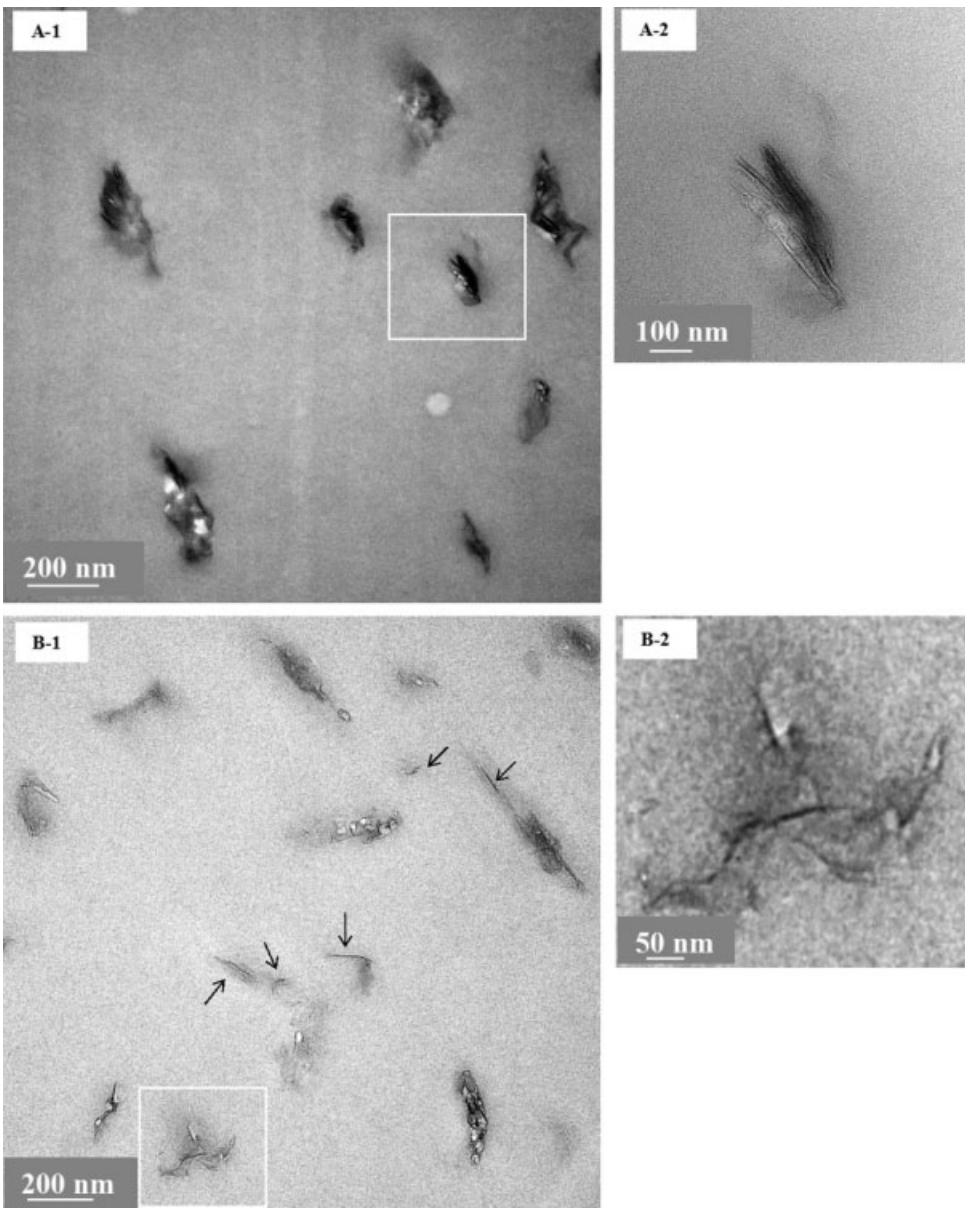

Figure 7 Transmission electron microscopy pictures showing the dispersion of oHT in (A1,A2) PS–oHT and (B1,B2) SAN–oHT. Arrows indicate exfoliated platelets.

these T_g values. The significant decrease in the both the Vicat softening temperature and T_g is a clear sign of the plasticizing effect promoted in the polymer matrix by the hybrid HT particles, and this is also in good agreement with the FTIR spectroscopy results discussed previously.

Tensile properties

Figure 8 presents the stress–strain tensile curves for all the materials. The tensile behavior of PS seems unaltered when oHT particles are incorporated. Only a slight increase in E can be observed (Table II). On the contrary, oHT particles seem to remarkably

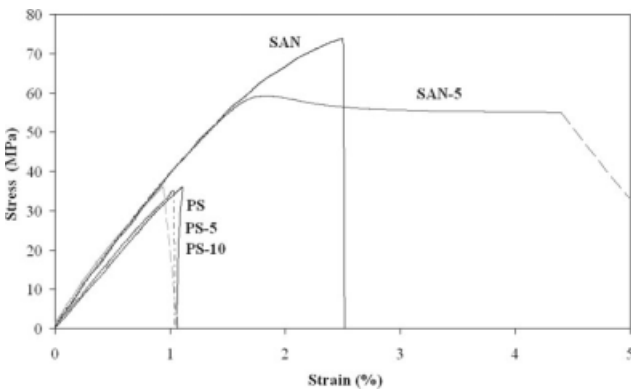

Figure 8 Typical tensile plots of the pure polymers and respective oHT nanocomposites.

TABLE II
Tensile Characteristics of the Pure Polymers and Composites

Material	E (GPa)	Tensile yield strength (MPa)	ε_b (%)
PS	3.4 (0.1)	38.3 (1.9)	1.1 (0.1)
PS-5	3.6 (0.1)	40.0 (3.4)	1.3 (0.2)
PS-10	3.9 (0.4)	39.5 (3.1)	1.2 (0.2)
SAN	3.6 (0.1)	74.6 (2.8)	2.5 (0.3)
SAN-5	4.3 (0.2)	59.0 (0.6)	4.1 (0.7)

The numbers in parentheses indicate the standard deviations.

increase SAN's ductility in terms of ε_b and reduce σ_{max}. This composite also shows a higher stiffness enhancement due to oHT particles in comparison with PS. This can be understood as mechanical evidence of better oHT particle dispersion in the SAN matrix versus PS. A relatively weak particle–matrix interface adhesion for the SAN composite, besides SAN's inherent high deformability, promotes oHT particle debonding at low stress levels and subsequent plastic flow of the formed polymer microfibrils. As a result, σ_{max} decreases and ε_b increases with respect to unfilled SAN.

K_{Ic}

The LEFM fracture parameters (K_{Ic} and G_{Ic}) were determined from three-point-bending fracture tests. Typical load–displacement plots are displayed in Figures 9. and 10 for all the tested materials First, an analysis of the elastic fracture linearity behavior was carried out according to the standard procedure; that is, only a maximum linearity deviation of 10% was accepted:

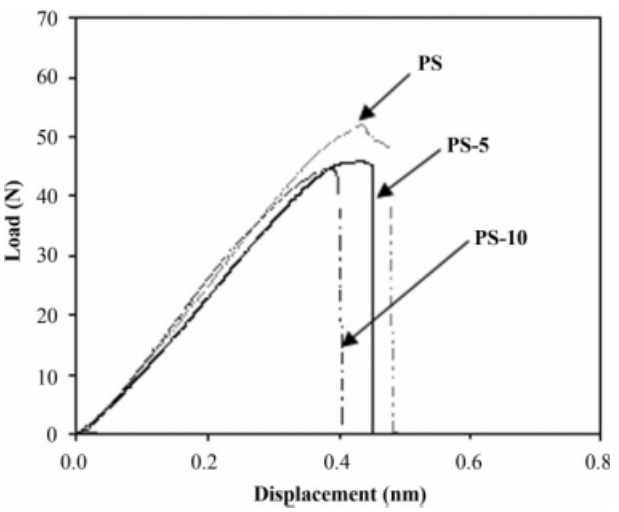

Figure 9 Typical fracture plots of PS and PS–oHT nanocomposites.

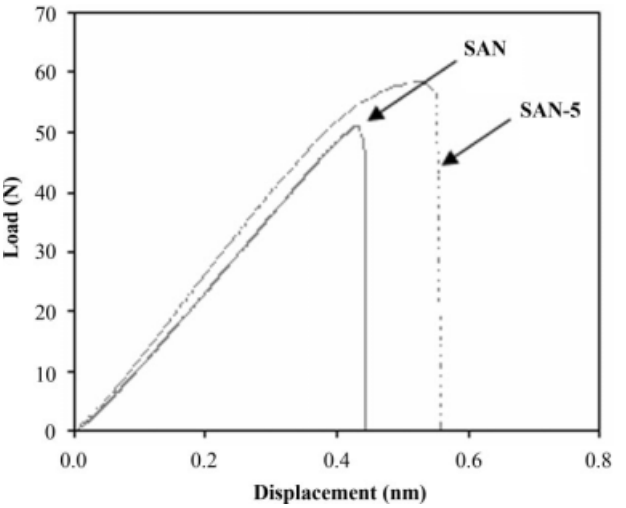

Figure 10 Typical fracture plots of the SAN copolymer and SAN–oHT nanocomposite.

$$\frac{P_{max}}{P_{5\%}} \leq 1.1 \quad (1)$$

where P_{max} is the maximum load value and $P_{5\%}$ is the load value at the intersection point of the modified compliance line with the experimental load–displacement plot. The results of the linearity analysis, as well as the calculated values of both K_{Ic} and G_{Ic}, are compiled in Table III. The minimum specimen thickness (B) necessary to guarantee plain-strain conditions at the crack tip, according to the usually used criteria, is also summarized:

$$\frac{2,5K_{Ic}^2}{\sigma_y^2} \leq B \quad (2)$$

The uniaxial tensile stress (σ_y) values correspond to the maximum stress value determined experimentally.

In view of these results, the two base polymers and respective composites fulfilled the LEFM linearity condition. All the SENB fracture samples, except that of pure PS, had the required specimen thickness to ensure that the critical stress intensity factor (K_{Ic}) was obtained under plain-strain conditions, that is, that the value corresponded to the material's K_{Ic} value.

Concerning the fracture parameters of the composites, a similar trend was observed for both K_{Ic} and G_{Ic}: PS's K_{Ic} and G_{Ic} values were slightly reduced when oHT particles were incorporated (Table III). This could be explained by the poor particle dispersion in these composites and by a weak interface between the PS matrix and the oHT particles. Although the plastic deformation mechanism of crazing, commonly observed in PS, was slightly

TABLE III
Results of the LEFM Fracture Analysis

Material	$P_{max}/P_{5\%}$	K_{Ic} (MPa $m^{1/2}$)	U_Q (N mm)	U_{cor} (N mm)	G_{Ic} (kJ/m^2)	$2.5K_{Ic}^2/\sigma_y^2$ (mm)
PS	1.01 (0.01)	1.55 (0.11)	8.22 (1.73)	0.76 (0.20)	0.96 (0.15)	4.1
PS-5	1.02 (0.01)	1.32 (0.17)	9.25 (2.98)	0.86 (0.10)	0.88 (0.30)	2.7
PS-10	1.02 (0.01)	1.37 (0.08)	8.23 (0.23)	1.00 (0.02)	0.76 (0.02)	3.0
SAN	1.02 (0.02)	1.43 (0.18)	6.86 (0.91)	0.91 (0.55)	0.67 (0.22)	0.9
SAN-5	1.06 (0.03)	2.17 (0.15)	19.32 (5.06)	2.23 (0.21)	2.06 (0.34)	3.4

The numbers in parentheses indicate the standard deviations.

affected by the presence of such particles, as shown in the fracture surface observed by scanning electron microscopy [shown later in Fig. 12(b)], this contribution did not seem to be enough to overlay the negative ones stated previously.

On the contrary, remarkable improvements in both K_{Ic} (50%) and G_{Ic} (200%) were found for the SAN composite with respect to the pure polymer. As seen on the composite fracture surfaces shown later in Figure 12, crack propagation passes through the particle–matrix interface (adhesive fracture). Two of the main factors affecting K_{Ic} in particulate-filled composites are the interface shear strength and the interface fraction in the composite. Although platelet exfoliation was not clearly observed for this composite, a slightly better dispersion of the oHT particles could explain this enhancement, the opposite of what was observed for the PS composites. It has been reported that the addition of inorganic particles can increase G_{Ic} of glassy polymers[19,38] and stabilize the crack propagation of semicrystalline polymers showing ductile instability.[39–41] In the case of the SAN composite, this remarkable increase in G_{Ic} can be attributed to plastic microdeformation during the fracture onset induced by the oHT platelets.

To compare the G_{Ic} value obtained from the energy used during the fracture test up to the crack growth onset [eq. (3)] with Griffith's fracture criterion,[42] a theoretical fracture energy value (G_{Ic}^*) was directly calculated with the material's E, Poisson's ratio (υ), and K_{Ic} values [eq. (4)]:

$$G_{Ic} = \frac{U}{BW\phi} \tag{3}$$

$$G_{Ic}^* = \frac{K_{IC}^2}{E}(1 - v^2) \tag{4}$$

where B and W are the thickness and width of the specimen, respectively, and ϕ is a dimensionless initial crack length-dependent geometry calibration factor. In the previous equations, U is the stored fracture strain energy corrected with consideration of the rod's indentation contribution and the machine compliance:

$$U = U_Q - U_{cor} \tag{5}$$

where U_Q is the energy up to the same load point used for K_{IC} and U_{cor} is the corrected energy.

Despite the quantitative differences between the two fracture energy values (G_{Ic} and G_{Ic}^*) shown in Figure 11 for all the composites and respective pure polymers, the global tendency regarding the material composition stayed unaltered.

Fractographic analysis carried out on both pure polymers revealed a smooth surface usually associated in glassy polymers with a brittle crazing type of fracture [Fig. 12(a,c)]. In filled glassy polymer systems, multiple crazing can be induced as an energy dissipation mechanism because crazes are able to initiate and end at the second phase particles. Comparatively, the fracture surfaces of the several composites are somewhat rough as a result of extensive polymer microdeformation [Fig. 12(b,d)]. Modified oHT particles seem to act as multiple crazing inducers. A more detailed composite fracture surface analysis allows us to say that PS–oHT's roughness is the direct result of combining a low stress value of craze formation with a weak interface. In this way, the G_{Ic} dissipation in PS–oHT can be explained by a combined multiple crazing phenomenon and a microvoiding mechanism due to particle debonding. Similar deformation mechanisms seem to be behind the fracture surface observed for the SAN–oHT composite. In this case, more extended microplastic

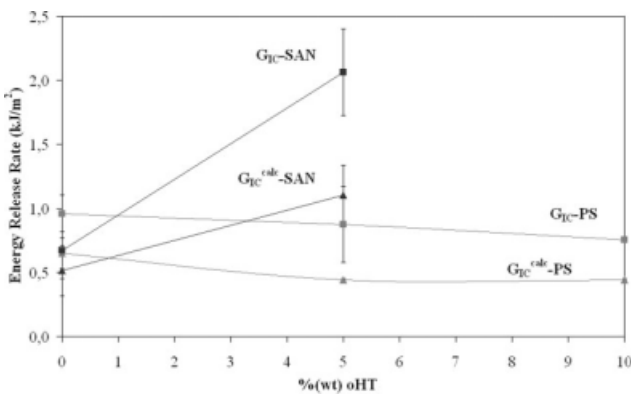

Figure 11 Comparison of the critical energy release rates obtained for the pure polymers and their respective HT nanocomposites.

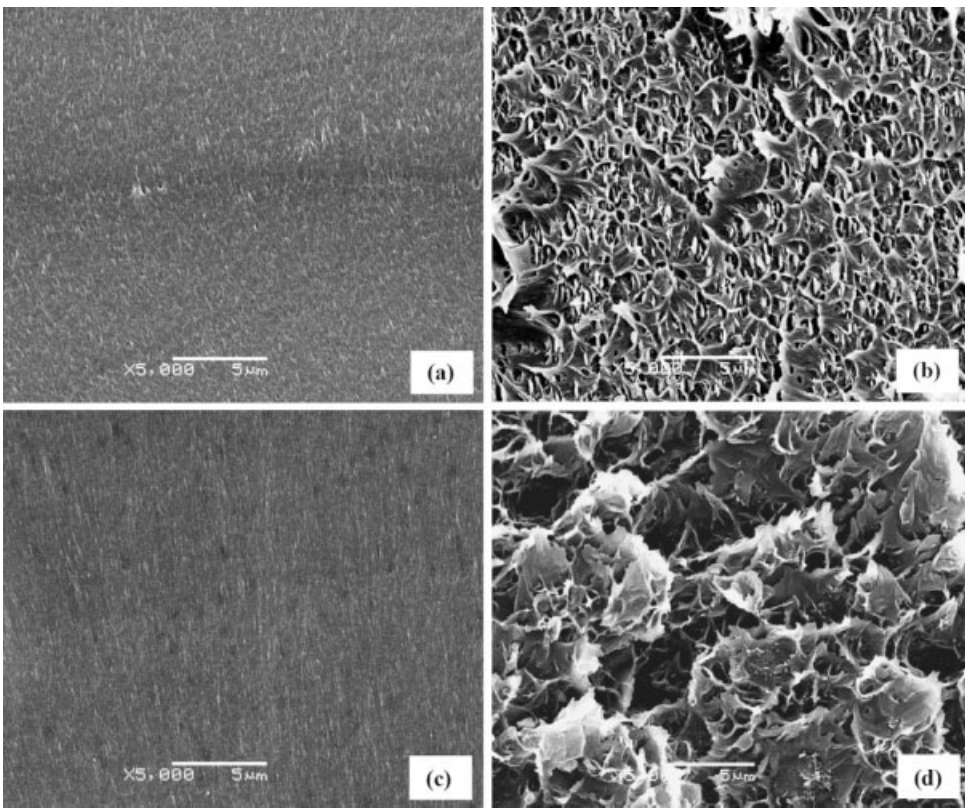

Figure 12 Scanning electron microscopy pictures showing the fracture surfaces of (a) PS, (b) PS-5, (c) SAN, and (d) SAN-5.

deformation has accompanied microvoid formation. This difference between SAN and PS oHT composites seems to be a direct result of SAN's inherently higher ductility. The combination of multiple crazing with microfibril plastic deformation has been found to be an effective K_{Ic} reinforcement mechanism for SAN.

CONCLUSIONS

Intercalated composites of PS and SAN with a DDS-modified Mg–Al HT were prepared by the melt-mixing method. Both the morphology and the mechanical and fracture properties were studied. The results showed that the previously ionically interchanged organic anions located in the interlayer of the LDH platelets acted as plasticizers for both styrenic polymers, reducing T_g by 5°C. The SAN–oHT composite showed an oHT disordered/intercalated type of structure, whereas an ordered/intercalated one was observed for PS–oHT composites. The different viscosities for the two base polymers seemed the most probable cause for all the structure differences between the PS- and SAN-based composites. In particular, the SAN–oHT nanocomposite showed increased ductility as well as a higher K_{Ic} value in comparison with the pure polymer, as revealed by tensile and LEFM fracture testing.

References

1. Qiu, L. Z.; Qu, B. J. J Colloid Interface Sci 2006, 301, 347.
2. Ding, P.; Qu, B. J. J Appl Polym Sci 2006, 101, 3758.
3. Qiu, L. Z.; Chen, W.; Qu, B. J. Colloid Polym Sci 2005, 283, 1241.
4. Leroux, F.; Meddar, L.; Mailhot, B.; Morlat-Therias, S.; Gardette, J. L. Polymer 2005, 46, 3571.
5. Qiu, L. Z.; Chen, W.; Qu, B. J. Polym Degrad Stab 2005, 87, 433.
6. Xu, Z. P.; Saha, S. K.; Braterman, P. S.; D'Souza, N. Polym Degrad Stab 2006, 91, 3237.
7. Lin, Y. J.; Wang, J. R.; Evans, D. G.; Li, D. Q. J Phys Chem Sol 2006, 67, 998.
8. Costa, F. R.; Satapathy, B. K.; Wagenknecht, U.; Weidisch, R.; Heinrich, G. Eur Polym J 2006, 42, 2140.
9. Costa, F. R.; Abdel-Goad, M.; Wagenknecht, U.; Heinrich, G. Polymer 2005, 46, 4447.
10. Ding, P.; Qu, B. J. Polym Eng Sci 2006, 46, 1153.
11. Pucciariello, R.; Tammaro, L.; Villani, V.; Vittoria, V. J Polym Sci Part B: Polym Phys 2007, 45, 945.
12. Kuila, T.; Acharya, H.; Srivastava, S. K.; Bhowmick, A. K. J Appl Polym Sci 2007, 104, 1845.
13. Du, L. C.; Qu, B. J. Polym Compos 2007, 28, 131.
14. Liao, C. S.; Ye, W. B. Electrochim Acta 2004, 49, 4993.
15. Wang, G. A.; Wang, C. C.; Chen, C. Y. Polym Degrad Stab 2006, 91, 2443.
16. Chen, W.; Qu, B. J. Polym Degrad Stab 2005, 90, 162.
17. Li, L.; Ma, R. Z.; Ebina, Y.; Iyi, N.; Sasaki, T. Chem Mater 2005, 17, 4386.
18. Utracki, L. A.; Sepehr, M.; Boccaleri, E. Polym Adv Technol 2007, 18, 1.

19. Johnsen, B. B.; Kinloch, A. J.; Mohammed, R. D.; Taylor, A. C.; Sprenger, S. Polymer 2007, 48, 530.
20. Kinloch, A. J.; Taylor, A. C. J Mater Sci 2006, 41, 3271.
21. Tjong, S. C. Mater Sci Eng R 2006, 53, 73.
22. Jordan, J.; Jacob, K. I.; Tannenbaum, R.; Sharaf, M. A.; Jasiuk, I. Mater Sci Eng A 2005, 393, 1.
23. Luo, J. J.; Daniel, I. M. Compos Sci Technol 2003, 63, 1607.
24. Kinloch, A. J.; Taylor, A. C. J Mater Sci Lett 2003, 22, 1439.
25. Liang, J. Z. J Appl Polym Sci 2002, 83, 1547.
26. Bartczak, Z.; Argon, A. S.; Cohen, R. E.; Weinberg, M. Polymer 1999, 40, 2347.
27. Thio, Y. S.; Argon, A. S.; Cohen, R. E.; Weinberg, M. Polymer 2002, 43, 3661.
28. Argon, A. S.; Cohen, R. E. Polymer 2003, 44, 6013.
29. Shah, D.; Maiti, P.; Gunn, E.; Schmidt, D. F.; Jiang, D. D.; Batt, C. A.; Giannelis, E. R. Adv Mater 2004, 16, 1173.
30. Shah, D.; Maiti, P.; Jiang, D. D.; Batt, C. A.; Giannelis, E. P. Adv Mater 2005, 17, 525.
31. Williams, J. G. A Linear Elastic Fracture Mechanics (LEFM) Standard for Determining K_{Ic} and G_{Ic} for Plastics: The Test Protocol; European Structural Integrity Society: Turin, Italy, 2001; p 14.
32. Richardson, M.; Braterman, P. J Phys Chem C 2007, 111, 4209.
33. Nakashima, K.; Ren, Y.; Nishioka, T.; Tsubahara, N.; Noda, I.; Ozaki, Y. J Phys Chem B 1999, 103, 6704.
34. Chen, G.; Liu, S.; Zhang, S.; Qi, Z. Macromol Rapid Commun 2000, 21, 746.
35. Qiu, L.; Chen, W.; Qu, B. Polym Degrad Stab 2005, 87, 433.
36. Csernica, J.; Brown, A. J Chem Educ 1999, 76, 1526.
37. Stretz, H.; Paul, D. Polymer 2006, 47, 8123.
38. Zunjarrao, S. C.; Sriraman, R.; Singh, R. P. J Mater Sci 2006, 41, 2219.
39. Velasco, J.; Saja, J.; Martinez, A. Fatigue Fract Eng M 1997, 20, 659.
40. Velasco, J.; Morhain, C.; Arencon, D.; Santana, O.; Maspoch, M. Polym Bull 1998, 41, 615.
41. Morhain, C.; Velasco, J. J Mater Sci 2001, 36, 1487.
42. Kinloch, A. J.; Young, R. J. Fracture Behavior of Polymers; Ellis Horwood: Chichester, England, 1983; Chapter 2.